ARTICLE IN PRESS

Journal of the European Ceramic Society xxx (xxxx) xxx–xxx

Contents lists available at ScienceDirect

Journal of the European Ceramic Society

journal homepage: www.elsevier.com/locate/jeurceramsoc

Towards enhanced sintering resistance: Air-plasma-sprayed thermal barrier coating system with porosity gradient

Bowen Lv, Xueling Fan, Dingjun Li, T.J. Wang*

State Key Laboratory for Strength and Vibration of Mechanical Structures, School of Aerospace Engineering, Xi'an Jiaotong University, Xi'an 710049, China

ARTICLE INFO

Keywords:
Sintering resistance
Thermo-mechanical analysis
Evaluation parameter
Porosity gradient
Thermal barrier coating

ABSTRACT

Sintering is one of the major failure mechanisms of air-plasma-sprayed thermal barrier coating system (APS TBCs) during high temperature service. For better sintering resistance, the TBCs with compositional gradient has been developed and fabricated by using advanced feedstocks, e.g. rare earth element-doped and nanostructured powders. Herein, a structurally graded design is put forward to counteract the effect of sintering in a convenient and economic way. Sintering induced degradations, in terms of Young's modulus and thermal conductivity, are slower in graded porous TBCs, indicated by thermo-mechanical finite element analyses and verified by experiments. Furthermore, a new sintering resistance parameter is proposed to evaluate the sintering resistance of TBCs under experimental (isothermal) and service (thermally graded) conditions. It is shown that graded porous TBCs, with decreasing porosity from top to bottom, exhibits improved sintering resistance and overall performance for engineering application.

1. Introduction

Advanced gas turbine, with increasing in-let gas temperature for higher efficiency, is regarded as a feasible solution to energy and environmental problems. As one of the key technologies for thermal protection, air-plasma-sprayed (APS) thermal barrier coating system (TBCs) is widely used in industrial gas turbines. Sintering is one of the major failure mechanisms of APS TBCs at elevated operation temperature [1–3]. Sintering of the ceramic layer in TBCs leads to microstructural evolution, densification, thermal and mechanical degradation, etc. [4–12]. In order to counteract the effect of sintering, functionally graded TBCs has been developed by incorporating advanced feedstocks. Rare earth zirconates, such as lanthanum zirconate (LZ) and gadolinium zirconate (GZ), have been applied with conventional yttria-stabilized zirconia (YSZ) to prepare double ceramic layer coating systems, commonly known as LZ/YSZ TBCs and GZ/YSZ TBCs [13,14]. Sintering resistance is improved because of the low diffusion rate of these doped rare earth elements [15]. Besides, there are increasing attentions devoted to nanostructured coating due to enhanced sintering resistance by the mechanism of differential sintering [16]. Fast sintering of nano-zone creates coarse pore in the microstructure, keeping a relatively constant porosity level and low sintering rate [17]. Recently, compositionally graded coatings have been developed with multi-layered structure based on these two kinds of powders [18,19]. However, these coatings are prone to premature failure due to fabrication issues [20]. Moreover, utilization of advanced powders in TBCs is limited for confidential and economic reasons for industrial gas turbines.

Structural design may provide an inspiring solution to challenges mentioned above. As reported in previous work [21], porosity is one of the key parameters controlling the sintering behavior of TBCs. Two approaches are currently available to introduce porosity gradient into the conventional YSZ TBCs: employing fuse-crushed/hollow spherical powders and adjusting spraying parameters [22,23]. In contrast to the first approach, the second one is more attractive to engineering application, for the reason of simple feedstock. TBCs with porosity gradient was produced by Portinha et al. [24] with modification of deposition parameters. Microstructure and microhardness were examined in the as-sprayed condition. In addition, microhardness distribution was also evaluated after 100 h annealing at 1100 °C. They not only observed porosity change as a function of spraying distance and power, but also obtained a relation between porosity and hardness. Moskal et al. [23] and Swadźba et al. [25] measured the residual stress in APS TBCs with porosity gradient manufactured by modifying spraying parameters. By comparing to the one with chemical gradient, they concluded that the former is more effective in application. Nevertheless, limited studies on the sintering behavior of APS TBCs with porosity gradient are reported to the best of our knowledge.

The objective of this work is to elucidate the effect of porosity gradient on sintering resistance. The design and numerical analysis of

* Corresponding author.
E-mail address: wangtj@mail.xjtu.edu.cn (T.J. Wang).

https://doi.org/10.1016/j.jeurceramsoc.2017.12.008
Received 26 July 2017; Received in revised form 27 November 2017; Accepted 6 December 2017
0955-2219/ © 2017 Elsevier Ltd. All rights reserved.

Please cite this article as: Lv, B., Journal of the European Ceramic Society (2017), https://doi.org/10.1016/j.jeurceramsoc.2017.12.008

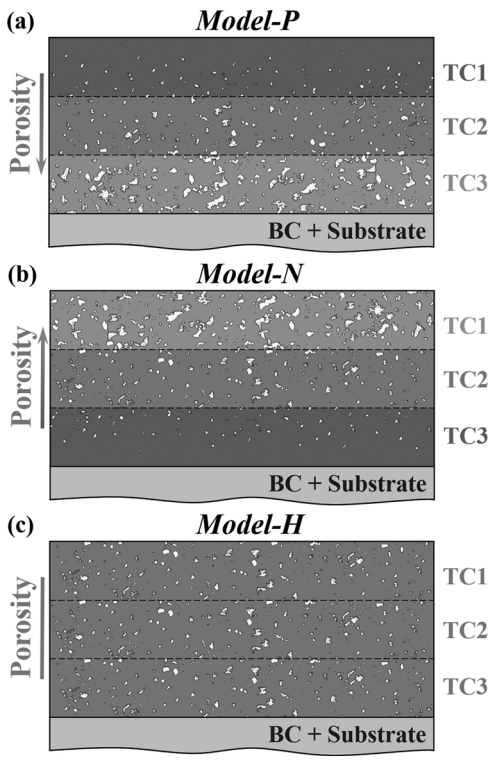

Fig. 1. Schematic of TBCs with different porosity gradient in top coat: (a) positive gradient (Model-P) with increasing porosity from top to bottom, (b) negative gradient (Model-N) with decreasing porosity, (c) homogeneous porosity (Model-H) with uniform porosity distribution.

APS TBCs with porosity gradient is presented in Section 2. Experimental verifications are described in Section 3. A parameter for the evaluation of sintering resistance is proposed in Section 4, along with the application in service condition. Concluding remarks are drawn in Section 5.

2. Design and analysis of graded porous TBCs

2.1. Structural design of graded porous TBCs

Functionally graded material (FGM) was initially proposed as thermal barrier material for space structures [26] and was extensively investigated [27–32]. Herein, this concept is extended to the microstructure of conventionally homogenous TBCs that is tailored by introducing the porosity gradient, in order to improve the sintering resistance of TBCs. Generally, TBCs with better strain compliance and thermal insulation is regarded as more sintering resistant. To this end, the reduction of Young's modulus and thermal conductivity, due to the introduction of porosity gradient, is discussed in the following preliminary theoretical derivations.

The graded porous TBCs can be simplified as an n-layered film-substrate system, as shown in Fig. 1. Herein, we take $n = 3$ in our analysis. Assume that the difference of Young's modulus between two adjacent layers is identical, being E_d, and the arithmetic average value of the whole system is E_m. As a result, the Young's modulus of the kth layer can be expressed as $E_k = E_m + [k - (n + 1)/2]\cdot E_d$. In addition, h_d denotes the distance from the film/substrate interface to the neutral axis of the film and h is the thickness of each layer. The equilibrium of axial forces under the three-point bending condition [33] dictates that

$$\sum_{k=1}^{n} \int_{(k-1)h-h_d}^{kh-h_d} E_k \frac{y}{R} \mathrm{d}y = 0 \tag{1}$$

where y is the distance to the neutral axis and R being the radius of curvature. h_d can be solved [34] from Eq. (1) and expressed as:

$$h_d = \left[\frac{(n^2 - 1)E_d}{12E_m} + \frac{n}{2}\right]\cdot h \tag{2}$$

According to the definition of effective bending stiffness [33], the effective Young's modulus E_{eff} of the layered system is related to the Young's modulus of each layer, namely

$$\int_{-h_d}^{nh-h_d} E_{eff} y^2 \mathrm{d}y = \sum_{k=1}^{n} \int_{(k-1)h-h_d}^{kh-h_d} E_k y^2 \mathrm{d}y \tag{3}$$

Submitting Eqs. (2) into (3) gives the expression of the effective Young's modulus:

$$E_{eff} = \frac{12n^2E_m^2 - (n^2 - 1)^2E_d^2}{12n^2E_m^2 + (n^2 - 1)^2E_d^2}\cdot E_m \tag{4}$$

with $(n^2 - 1)^2E_d^2 \geq 0$ and consequently $[12n^2E_m^2 - (n^2 - 1)^2E_d^2]/[12n^2E_m^2 + (n^2 - 1)^2E_d^2] \leq 1$. Therefore, the effective Young's modulus is inferior or equal to the arithmetic average value. Combination of graded layers leads to the lower overall stiffness. The reduction is more evident with more significant gradient. The lower limit of the effective Young's modulus is $[(2n^2 - 2n - 1)/(4n^2 + 2n + 1)]\cdot E_m$, when E_d approaches its maximum value of $2E_m/(n - 1)$. If n tends to infinity, the layered system turns to be continuous, with a linear distribution of Young's modulus along the cross-section. In this case, the lower limit is simplified as $E_m/2$, which is in agreement with the result obtained by integration. If there is no gradient, $E_d = 0$ and Eq. (4) reduces into $E_{eff} = E_m$.

On the other hand, the heat transfer problem of layered system can be simplified as a fixed temperature on the upper boundary and a constant heat flow in the through-thickness direction. Similar to the derivation of effective Young's modulus, the thermal conductivity of the kth layer is $\lambda_k = \lambda_m + [k - (n + 1)/2]\cdot\lambda_d$, where λ_m is the arithmetic average value and λ_d is the difference between two adjacent layers. Again, h is the thickness of each layer. According to the Fourier's law [35], thermal conductivity is defined as the function of heat flux ($\dot{q}_h$) and temperature gradient ($\mathrm{d}T/\mathrm{d}y$):

$$\frac{\dot{q}_h}{\lambda} = -\frac{\mathrm{d}T}{\mathrm{d}y} \tag{5}$$

Considering the unidirectional conduction process [36], the integration of Eq. (5) over the cross-section gives:

$$\int_{0}^{nh} \frac{\dot{q}_h}{\lambda_{eff}} \mathrm{d}y = \sum_{k=1}^{n} \int_{(k-1)h}^{kh} \frac{\dot{q}_h}{\lambda_k} \mathrm{d}y \tag{6}$$

Assuming n is an odd number, the effective thermal conductivity (λ_{eff}) of this n-layered system can be written as follows, by summing the kth and the $(n + 1\text{-}k)^{\text{th}}$ terms:

$$\frac{n}{\lambda_{eff}} = \frac{1}{\lambda_m} + \sum_{k=1}^{(n-1)/2} \frac{2\lambda_m}{\lambda_m{}^2 - \lambda_d{}^2[k - (n + 1)/2]^2} \geq \frac{1}{\lambda_m} + \sum_{k=1}^{(n-1)/2} \frac{2}{\lambda_m} = \frac{n}{\lambda_m} \tag{7}$$

It should be noted that $\lambda_d{}^2[k - (n + 1)/2]^2 \geq 0$. Therefore, $\lambda_{eff} \leq \lambda_m$, according to Eq. (7). This result can be similarly obtained in the case of n being an even number. The effective thermal conductivity of the layered system is lower than or equal to the arithmetic average value. Introduction of graded layers improves the general thermal insulation. The larger is the gradient, the lower is the effective thermal conductivity. With the gradient approaching the maximum limit, λ_d turns to $2\lambda_m/(n - 1)$, resulting in the minimum limit of λ_{eff} being 0. When there is no gradient, λ_d is null and λ_{eff} reduces into λ_m, according to Eq. (7).

As mentioned in Section 1, previous studies mainly focused on advanced feedstocks for enhanced sintering resistance. Nevertheless, introducing new powders in spraying process is complicated and expensive. Seeing that porosity plays important roles not only in the mechanical and thermal properties, but also in the sintering behavior of

TBCs [21], we propose a structural design of porosity gradient to counteract the sintering effect in this study. The graded porous TBCs has the porosity distribution varying in the through-thickness direction. For simplification, the whole coating is discretized into three sublayers with high, moderate and low porosity levels, as shown in Fig. 1. Specifically, positively graded samples (Model-P) refer to the ceramic coatings with porosity increasing from top to bottom. Negatively graded samples (Model-N) refer to those with inverted microstructure. Homogeneous porous coatings (Model-H) are for reference purposes.

2.2. Numerical analysis framework

Fully coupled thermo-mechanical sintering behavior of TBCs can be predicted by finite element analysis (FEA), especially in the complex service condition with non-uniform temperature distribution. A thermally coupled elasto-viscoplastic constitutive model has been developed to describe the sintering behavior of APS TBCs at elevated temperature:

$$\{d\varepsilon\} = \{d\varepsilon^{E}\} + \{d\varepsilon^{Vp}\} + \{d\varepsilon^{sint}\} + \{d(\alpha T)\} \tag{8}$$

where $d\varepsilon$ is the total strain increment, $d\varepsilon^{E}$ is the elastic strain interment, $d\varepsilon^{Vp}$ is the viscous plastic strain increment, $d\varepsilon^{sint}$ is the free sintering strain increment and $d(\alpha T)$ is the thermal strain increment. The constitutive equation is expressed in the incremental form:

$$\{d\sigma\} = [D^{*}](\{d\varepsilon\} - [\eta]^{-1}\{\sigma\}dt - \{d\varepsilon^{sint}\} - d\{\alpha T\}) \tag{9}$$

with $[D^{*}]$ being the modified elastic matrix and $[\eta]$ being the viscous matrix. Note that most of the parameters in this model are related to the relative density ρ, which can be theoretically derived as a function of sintering time t, initial relative density ρ_0, viscosity η, initial pore radius R_0 and surface energy γ:

$$\int_{\rho_0}^{\rho} (1-\rho)^{-\frac{2}{3}}\rho^{-\frac{11}{3}}d\rho = \frac{3}{2}\left(\frac{\rho_0}{1-\rho_0}\right)^{-\frac{1}{3}}\frac{\gamma}{\eta k R_0}t \tag{10}$$

where k is a dimensionless constant obtained from experiment. Detailed expressions and derivations can be found in our previous work [21].

The effect of temperature on mechanical behavior is reflected through thermal stress in the constitutive relation above, but not vice versa. In order to describe the fully coupled thermo-mechanical response, the effect of mechanical evolution on thermal property needs to be taken into consideration. Experimental results indicate that viscosities of a variety of materials follow the Arrhenius relation as a function of temperature [37–39]. Specifically, the viscosity of YSZ strongly depends on temperature, with values of 144 GPa·h at room temperature and about 1 GPa·h at 1200 °C [40]. Hence, we assume the following relation by interpolation of viscosity data at 1200 °C and 1400 °C from the experiment of Ahrens et al. [40]:

$$\eta = 10.244 \times \exp[19831/(T + 273)], (1200 \le T \le 1400) \tag{11}$$

with η being viscosity in MPa·s and T being temperature in °C. Viscosity estimated by Eq. (11) is 16.58 GPa·h at 1000 °C, which is relatively close to the experimental measurement by Ahrens et al. [40] of approximately 12 GPa·h. Consequently, the combination of Eqs. (10) and (11) gives the relationship between temperature and relative density. Besides, previous experiments on APS TBCs show an approximately linear relation between thermal conductivity and porosity of YSZ when the latter is lower than 25%, which equals to a range of over 0.75 in relative density [41–43]. Based on experimental data by Bjorneklett et al. [44], thermal conductivity is assumed to be a linear function of relative density:

$$\lambda = -3.75(1-\rho) + 1.25, (0.75 \le \rho \le 0.95) \tag{12}$$

where λ is thermal conductivity in W/m/K and ρ the dimensionless relative density. In brief, sintering induced evolution of relative density depends on temperature and determines thermal conductivity. With heat transfer analysis correlating temperature field to thermal conductivity, the relation between mechanical behavior (densification driven by sintering stress) and temperature can be established. Thus, the fully coupled thermo-mechanical constitutive relation is developed.

The proposed constitutive relation is implemented into the commercial software ABAQUS. Mechanical properties and behaviors are coded in a user subroutine UMAT, detailed elsewhere [21]. To take the thermal effect into account, Eq. (11) is added in UMAT while Eq. (12) is coded in the user subroutine UMATHT describing thermal properties. Invoking these subroutines in the coupled temperature-displacement calculation procedure, coupled thermo-mechanical behavior can be analyzed. Four-node bilinear displacement and temperature element (CPE4T) is employed.

A plane strain model is built for the free-standing ceramic coating in a rectangular shape with a thickness of 200 μm and a width of 1 μm. Average relative density of TBCs is set 0.85 according to experimental observations. The difference of relative density between adjacent sublayers is 0.09 in graded porous coatings. Periodic condition [45–47] is applied on the left and right boundaries and the vertical displacement of the lower boundary is constrained. To compare with experimental results, analyses are conducted in a uniform temperature field of 1200 °C. This temperature is adopted to accelerate the sintering process, considering the long lifetime of APS TBCs at conventional working temperature. In the study of thermal conductivity during sintering, data are obtained according to Eq. (12) based on relative density evolution and are simultaneously recorded in output files of FE analyses. Normalization is conducted referring to the final value, for the purpose of showing the evolution tendency. To elucidate the effect of sintering on effective Young's modulus, uniform pressure is exerted periodically on the upper boundary in a sufficiently short loading cycle (2% of total analysis step), guaranteeing the accuracy of calculation. The displacements of the upper boundary at the start and at the end of each loading period are outputted under cyclic loading. Then the decrease in thickness and the change of strain are calculated. The effective Young's modulus is obtained by the incremental ratio of stress over strain and normalized by the final value. This Young's modulus is taken as the average value in the middle of loading period. Note that the sintering time is normalized by the final value of each calculation. In the last part of this work, temperature is fixed at upper boundary while constant heat flux flows out of the lower boundary, resulting in a through-thickness temperature gradient, for the simulation of service condition. Interfacial stress state is investigated by extracting the horizontal stress at the bottom of TC before the coating is fully-sintered. Normalization is carried out by the equivalent sintering stress obtained from the constitutive model [21].

2.3. Evolution of Young's modulus

Similar to previous results [12,48,49], Young's modulus increases significantly in a short period until reaching the plateau, as shown in Fig. 2. Focusing on the initial stage of sintering, Young's moduli of the graded porous coatings are 10.66% lower than that of the homogenous one, which is notable given that initial total porosity is similar in all coatings while only the distribution is different. The graded porous coatings are less stiff than the homogenous one, until all coatings are fully sintered in the late stage. Apart from the complex derivation in Section 2.1, the reduction can be straightforwardly explained as follows: the coating with homogenous microstructure has a uniform stress distribution on the cross-section thus the optimal load carrying capacity and Young's modulus; introducing a graded distribution, while keeping the average porosity, weakens the load carrying capacity and reduces the Young's modulus. Also, the reduction is positively related to porosity gradient. Maintaining sufficient toughness, microstructure with high porosity gradient is recommended, considering the enhanced strain tolerance for engineering application.

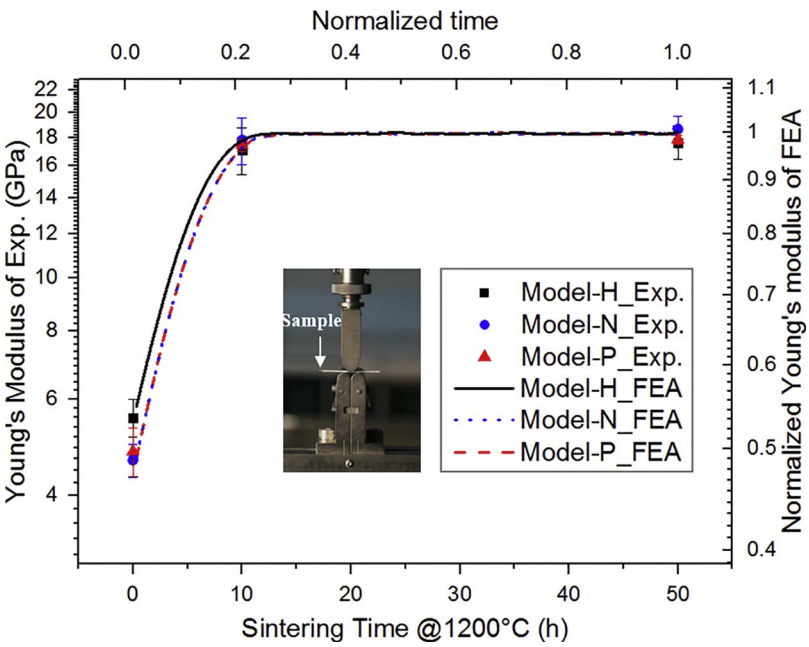

Fig. 2. Relation between Young's modulus and sintering time obtained from three-point bending tests, compared with that between normalized Young's modulus and normalized time obtained from finite element analyses (FEA).

2.4. Evolution of thermal conductivity

The evolution of thermal conductivity during annealing treatment is shown in Fig. 3. The increase of thermal conductivity induced by sintering is in agreement with previous studies [16,50,51], showing a fast initial stage before reaching the steady state. Only the results of Model-N and Model-H are plotted, seeing that evolution of Young's modulus is almost identical in two graded porous coatings, as discussed in Section 2.3. Theoretically, the sintering resistance of positively graded porous coating should be the same as negatively one under isothermal treatment. Comparison of thermal conductivities between homogeneous and graded porous coatings reveals ~10% reduction in the latter, which is significant for TBCs. Consequently, the graded porous TBCs is more thermally insulant than the conventionally homogenous coating during sintering. Note that the reduction of thermal conductivity is positively dependent on the porosity gradient. In addition to the derivation in Section 2.1, it is easily understood by referring to the equivalent resistance of parallel circuit.

3. Experimental verification

3.1. Preparation of TBCs samples with porosity gradient

TBCs samples with porosity gradient were produced from

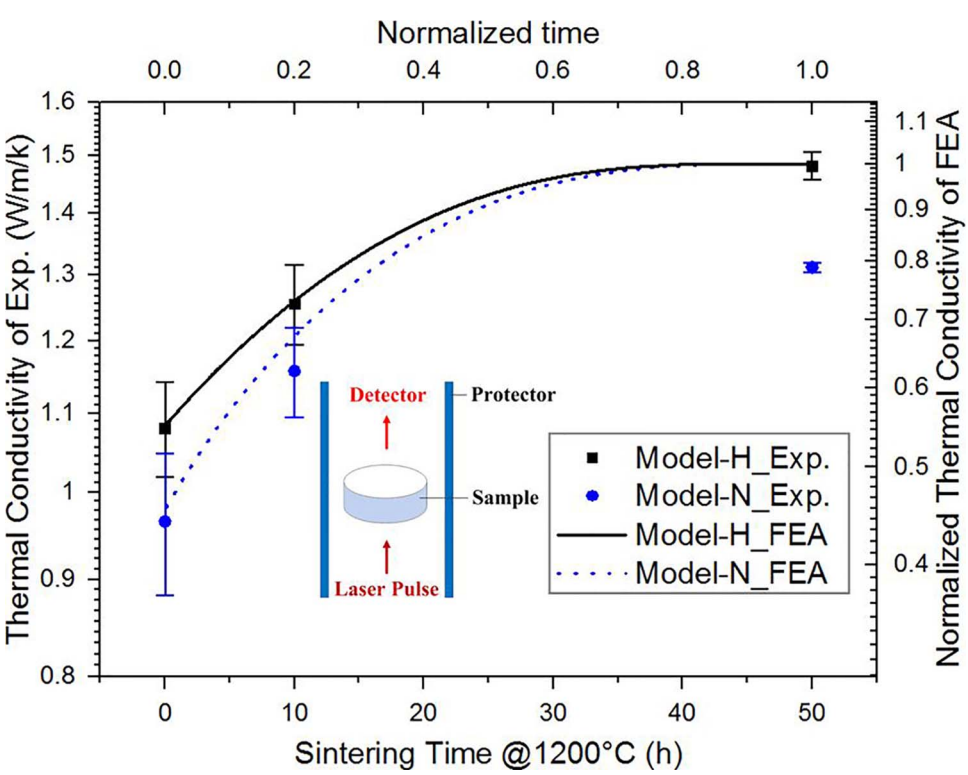

Fig. 3. Relation between thermal conductivity and sintering time obtained from laser-flash tests, compared with that between normalized thermal conductivity and normalized time obtained from finite element analyses (FEA).

Table 1
Deposition parameters for the fabrication of APS coatings with porosity gradient achieved by three sublayers, i.e. high, moderate and low porosity sublayers.

Deposition parameters	High porosity	Moderate porosity	Low porosity
Power (kW)	35.2	37	44.2
Int. of current (A)	565	545	600
Gas plasma (l/min)	40	40	40
Gas transport (Ar) (l/min)	2.8	2.5	2.5
Gas transport (H_2) (l/min)	6.5	8	12
Diameter of nozzle (mm)	8	8	6
Flux of powder (g/min)	56	40	40
Distance of gun to substrate (mm)	120	120	100
Substrate temperature (K)	400	400	400
Gun speed (mm/s)	500	500	500

commercial ZrO_2-8wt%Y_2O_3 powder (Metco 204NS, Oerlikon Metco, Winterthur, Switzerland), using plasma spray gun (F4MB-XL, Oerlikon Metco, Winterthur, Switzerland). Three types of ceramic coatings (Fig. 1) with different distributions of porosity were deposited, according to the spraying parameters summarized in Table 1.

Samples for microstructure characterization and three-point bending tests were sprayed on rectangular bars with the dimension of $45.0 \times 7.0 \times 1.3\,mm^3$. Bond coating was deposited beforehand using standard commercial CoNiCrAlY powder (Amperit 415, H.C. Starck, Germany) by high velocity oxygen fuel (HVOF) spraying system (JP8000, Praxair, Indianapolis, IN) on the sand blasted superalloy substrate (Haynes 230, Kokomo, IN). Free-standing ceramic coatings were obtained by bathing in hydrochloric acid for 6 h. Samples for thermal conductivity measurement were sprayed directly onto graphite disks, with a diameter of 12.7 mm and a thickness of 1.3 mm. Annealing treatment was conducted on free-standing samples in a high temperature muffle furnace (KSL-1700X, MTI Corp., China) at 1200 °C for different durations up to 50 h.

3.2. Microstructure characterization

Microstructures of as-sprayed and sintered samples were examined by FEI Quanta 400 (FEI, Hillsboro, OR) scanning electron microscope (SEM) operating in high vacuum mode. The coatings were embedded with epoxy resin beforehand, in order to reduce the possibility of damage. Cross-sections of the three types of coatings were polished using standard metallographic procedures and gold sputtered to acquire high quality SEM images. Image analysis was then performed using open-source software (Image J, U.S. National Institutes of Health). Thresholding of the SEM image yielded a binary image that facilitated the determination of void area. The percentage in the cross-section was taken as the total porosity. Furthermore, the porosity level of each sublayer was evaluated by analyzing the corresponding part of the cross-section, which shed light on the porosity distribution. Additionally, voids with the aspect ratio below 2 or over 20 were defined herein as round pores or microcracks, respectively. Based on the identification of different types of voids, the sintering induced microstructure evolution was further investigated. A total number of nine images were captured for analysis in each case.

3.3. Three-point bending test

The effective Young's moduli of as-sprayed and sintered TBCs were determined by three-point bending test, with a span of 10 mm, on free-standing samples at room temperature. A quasi-static load was applied by universal testing facility (MicroTester 5848, Instron, Norwood, MA) at the rate of 0.04 mm/min. The linear part of load-displacement curve was extracted to calculate the effective Young's modulus by the following equation:

$$E = \frac{SL^3}{4bh^3} \tag{13}$$

where S, L, b, h are respectively the slope of the linear part of load-displacement curve, span of the fixture, width and thickness of the sample. For each type of microstructure and sintering duration, three samples were tested to improve the statistics.

3.4. Laser-flash analysis

The through-thickness thermal diffusivity of TBCs with porosity gradient was measured by the laser-flash technique (LFA 427, Netzsch, Germany) in He atmosphere at room temperature (25.5 ± 0.5 °C) after different sintering durations, with laser voltage of 450 V and pulse width of 0.5 ms. Before each measurement, the average density of sample was examined by the Archimedes principle. Then thin layers of graphite were coated on both sides of sample, considering the translucency of YSZ. Specific heat capacity was established by differential scanning calorimeter in the same device. Overall thermal conductivity was calculated by the following equation:

$$\lambda = \alpha \cdot C_p \cdot \rho \tag{14}$$

where α is thermal diffusivity, C_p is specific heat capacity and ρ is density. Thermal conductivity was evaluated three times in each condition for statistical purposes.

3.5. Results and discussion

3.5.1. Microstructures

Porosity gradient was observed in the cross-sectional SEM images of as-sprayed free-standing TBCs. Denser microstructure was seen in the top sublayer while more pores existed in the bottom sublayer of Model-P, as shown in Fig. 4(a). As the result of reversed spraying sequence, the microstructure of Model-N exhibited the inverted porosity distribution (Fig. 4(b)). In addition, a uniform microstructure of Model-H was presented in Fig. 4(c). Microstructure features, such as inter-splat microcracks and round pores, were indicated in the figure as well. The typical length and thickness of splat are ~50 μm and ~5 μm, respectively. Furthermore, high spraying quality was achieved in graded porous coatings, without evident interface between sublayers. Consequently, the spallation of the outer sublayer in double-layer coatings [14,52] could possibly be avoided.

Evolutions of porosity distribution during sintering are plotted in Fig. 4(d)–(f). Largest porosity range, from top to bottom, was around 5% at as-sprayed state. This range, which could be expanded in the future for demanding applications, was sufficient to make a difference in the sintering resistance herein. After annealing treatment at 1200 °C for up to 50 h, porosity gradient was still preserved in the microstructure. In addition, the porosity range decreased slightly, except for Model-H. Porosity levels of the porous and dense sublayers in Model-P declined approximately by 1/5 and 1/10, respectively. Corresponding values were around 1/10 and 1/20 in Model-N. It is suggested that sublayers with higher porosity shrank faster, narrowing the range of porosity distribution. Note that the two graded porous coatings, i.e. Model-P and Model-N, should behave in the same way during isothermal annealing treatment, as also indicated by the results of finite element analysis in Section 2.

Evolution of total porosity, as the average on cross-section, is shown in Fig. 5(a). A relatively fast drop of total porosity level is seen in the first 10 h annealing treatment, followed by a quasi-static sintering behavior in the last 40 h. This result qualitatively agreed with the mercury porosimetry measurement by Siebert et al. [53]. In their experiment, fraction of pores bigger than 1 μm^2 decreased from around 18% to 15%, and then to 14% in the first and second 50 h of annealing treatment at 1100 °C, respectively. It should be pointed out that although porosity levels herein were slightly lower than commercial APS TBCs, analyses

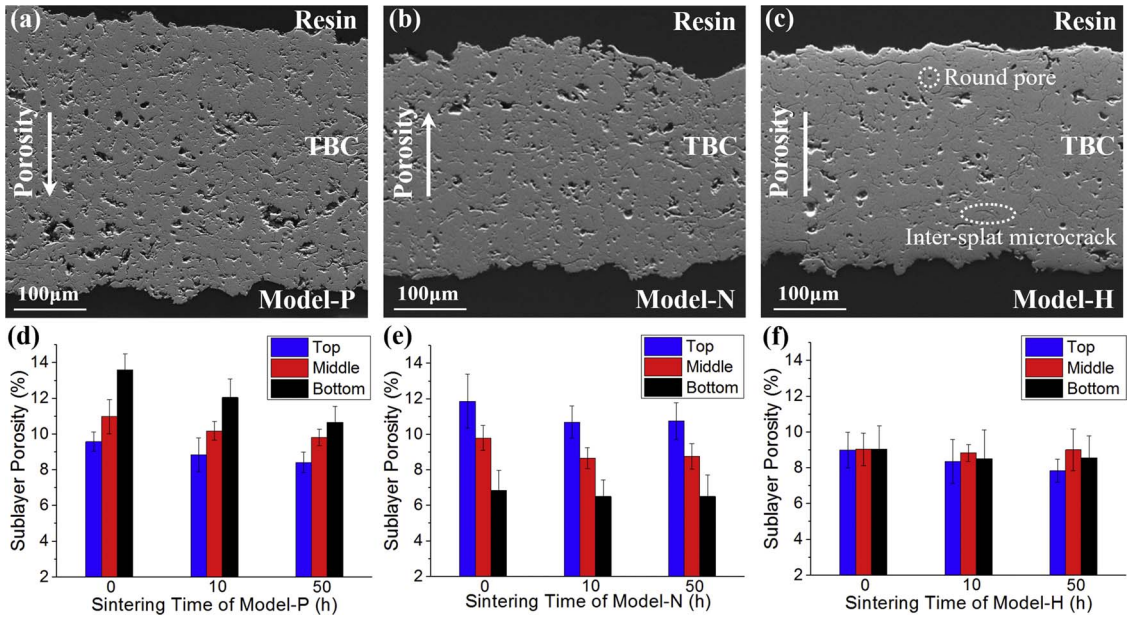

Fig. 4. SEM cross-sections of as-sprayed free-standing TBCs with different porosity gradients: (a) positive gradient (Model-P) with increasing porosity from top to bottom, (b) negative gradient (Model-N) with decreasing porosity, (c) homogeneous porosity (Model-H) with uniform porosity distribution; Porosity distributions of top, middle and bottom sublayers at different sintering time in (d) Model-P, (e) Model-N and (f) Model-H.

on the effect of porosity gradient could serve as a reference to all coatings. Additionally, the reduction in porosity is correlated with the densification of sample, which can be characterized by the through-thickness/in-plane shrinkage. The experiment by Paul et al. [54] recorded a fast shrinkage stage in the beginning of annealing treatment and subsequently a quasi-static one, which is in agreement with the porosity evolution in this work. Furthermore, comparison of porosity evolution curves suggests that Model-N had a comparable porosity

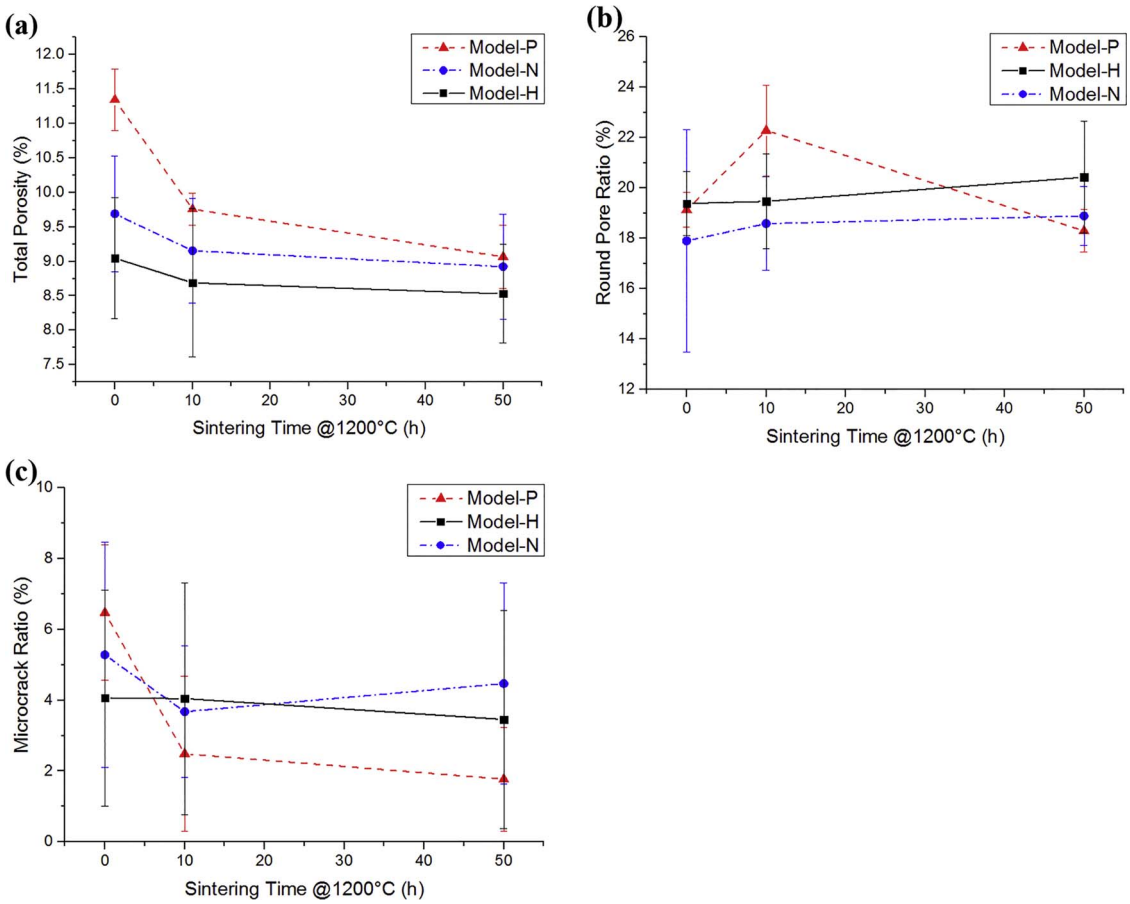

Fig. 5. (a) Evolution of total porosity during sintering of TBCs with graded and homogenous microstructures; Changes in pore shape during sintering were characterized by the ratios of round pore (b) and microcrack (c) to total porosity.

decreasing rate as Model-H, while the porosity of Model-P dropped about 2 times faster, probably due to the higher porosity level. In view of slower densification rate, it is inferred that coatings with negative porosity gradient may have better sintering resistance than the positively graded ones.

Besides total porosity evolution, it is of great interest to elucidate how the pore shape changes during sintering. It is seen from Fig. 5(b) that round pores constituted approximately 1/5 of total porosity. Considering the already low total density (~10%), the plot only serves to qualitatively show the trend of evolution, which will be further discussed below. Generally speaking, the proportion of round pores kept going up during sintering. On account of lowering Gibbs free energy, pores became round driven by surface tension (sintering stress). This phenomenon is the so-called pore spheroidization [4,9]. In addition, both graded porous coatings, i.e. Model-N and Model-P, showed a two-stage behavior. In the first 10 h, irregular-shaped pores became round under the effect of surface diffusion, leading to a fast increase of round pore ratio. Subsequently, the closure of round pores (especially the small ones) took place as the grain boundary diffusion became dominant, resulting in a slower increase or even a decrease in the late stage. In comparison, the pore spheroidization in Model-H is relatively steady, probably due to the homogenous microstructure.

Microcrack between splats is another feature of APS TBCs, owing to the spraying technique. As illustrated in Fig. 5(c), microcracks contributed less than 1/10 of total porosity and the proportion generally decreased during sintering. The reduction is attributed to the healing of crack tip driven by surface diffusion, as well as the cutting-off effect by sintering neck formation [55]. The slight increase in microcrack fraction in the last 40 h annealing treatment of Model-N may be the result of experimental uncertainty. One possible source could be the different samples used for the annealing treatments of different durations. Recall that they were embedded in epoxy resin for the microstructure characterization on polished cross-section, and that removing the sample from the resin could cause serious damage. Considering the small proportion of the specific microstructure features in the already low total porosity, a slight difference of sample microstructure could possibly lead to a non-negligible deviation, as shown in Fig. 5. A potential solution to minimize the deviation may be in-situ SEM during annealing treatment at high temperature, to which we currently have no access and plan to do it in the future. Besides, the image analysis is based on a limited number of cross-sectional images. Although with some other methods, such as mercury or water porosimetry, the total porosity can be measured as a function of pore size in the whole sample, it is difficult to investigate the local area and distinguish round pores from microcracks.

3.5.2. Mechanical and thermal properties

As shown in Fig. 2, the experimentally measured Young's modulus is in good agreement with the numerical result. According to the experimental measurement, Young's moduli of Model-P and Model-N were reduced by 13.23% and 16.45% in the initial stage, respectively. Note that the numerically predicted Young's moduli of both graded porous coatings were 10.66% lower than that of the homogenous one, as discussed in Section 2.3. In addition, the evolution of Young's modulus is inversely dependent on the reductions of the total porosity (Fig. 5(a)) and microcrack ratio (Fig. 5(c)), suggesting that pore shrinkage and microcrack healing are among the main reasons for the stiffening of coating. In contrast, pore spheroidization seems to play a less important role. The fracture faces of microcracks, mainly along the in-plane direction, have the potential to glide under the effect of bending moment, while the round pores make approximately the same contribution to the deformation as the irregular-shaped ones.

The experimental measurements of thermal conductivity generally agree with the result of finite element analysis, as shown in Fig. 3. Both experimental and numerical results indicated a reduction of over 10% in the initial stage. In contrast, the graded porous coatings showed a slower degradation in the late stage annealing treatment, comparing to the numerical prediction. The reason may be inter-splat or interfacial microcracks neglected by the FE model, which remains to be explored in future studies.

In brief, the introduction of porosity gradient leads to reductions of Young's modulus and thermal conductivity at as-sprayed state. The initially lower Young's modulus and thermal conductivity of graded porous TBCs keep inferior to those of conventionally homogenous coatings during sintering, which are related to the microstructure of coatings. Therefore, it is of great value to seek a criterion for the evaluation of sintering resistance, in consideration of structural evolution, so that redundant discussions can be avoided and more profound understanding of the sintering resistance can be achieved.

4. Sintering resistance evaluation

4.1. Evaluation parameter R_s

In previous studies, sintering resistances of different TBCs were commonly evaluated by comparing the changes in Young's modulus or thermal conductivity. Young's modulus is a simple but fundamental parameter describing the sintering resistances of different TBCs. Siebert et al. [53] measured the changes in Young's modulus of two different TBCs after annealing at 1100 °C for 2, 50 and 100 h. They concluded that the coating with slower increase of Young's modulus was more sintering resistant. In the experiment of Shinmi et al. [56], TBCs sintered at 1400 °C for up to 300 h was characterized by the measurement of Young's Modulus evolution. They observed increase of Young's modulus in the first 50 h because of sintering.

On the other hand, thermal conductivity is another key parameter to characterize the sintering of TBCs. Rätzer-Scheibe et al. [57] concluded from their experiment that the significant increase in thermal conductivity could be attributed to microstructural changes, induced by sintering in the first 100 h of annealing at 1100 °C. Yu et al. [58] found that the increase of thermal diffusivity was due to the effect of sintering, after annealing treatment for 34 h at 1050 °C.

Although these two parameters are straightforward and applicable in the study of sintering resistance, there is no clear criterion for sintering resistance evaluation up to now. Since sintering of TBCs is simultaneously related to mechanical and thermal properties, a criterion taking both of them into consideration is necessary for scientific research and engineering application. Moreover, Young's modulus and thermal conductivity are the key parameters for the mechanical and thermal performances of TBCs, respectively. Considering the changes of Young's modulus and thermal conductivity, we propose a dimensionless sintering resistance parameter R_s,

$$R_s = \frac{E_{ref}}{E} \cdot \exp\left(\frac{\lambda_{ref} - \lambda}{\lambda_{ref} + \lambda}\right) \tag{15}$$

where E and λ are the Young's modulus and the thermal conductivity of TBCs, respectively. The subscript *ref* denotes the corresponding parameters of conventional TBCs for reference. In addition, Eq. (15) can be applied to evaluate the sintering resistance of TBCs by referring to its initial state, which is not the major concern of this paper.

According to our previous work [21] and Eq. (12), Young's modulus and thermal conductivity can be expressed as functions of relative density ρ or porosity p, with $p = 1 - \rho$:

$$\begin{cases} E = E_0 \exp(-bp) \\ E_{ref} = E_0 \exp(-bp_{ref}) \end{cases} \tag{16}$$

$$\begin{cases} \lambda = \lambda_0 (c_1 - c_2 p) \\ \lambda_{ref} = \lambda_0 (c_1 - c_2 p_{ref}) \end{cases} \tag{17}$$

where b, c_1 and c_2 are positive constants determined by experimental data.

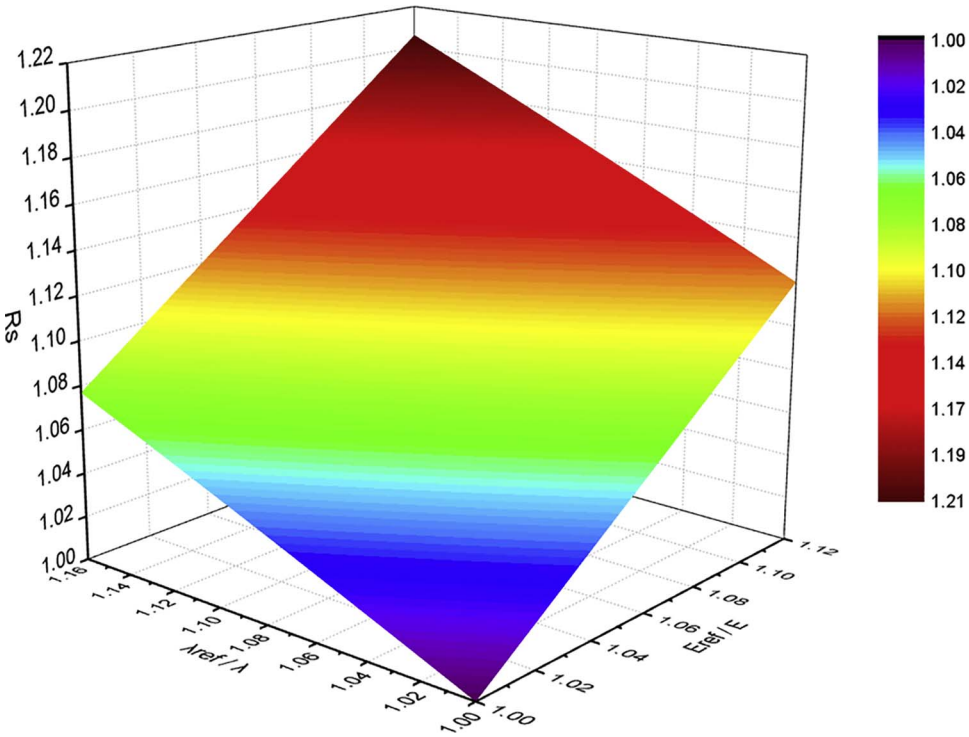

Fig. 6. Distribution of sintering resistance (R_s) in three-dimensional coordinate system constituted of Young's moduli and thermal conductivity ratios, reflecting the weight of these parameters in R_s.

Substitution of Eqs. (16) and (17) into Eq. (15) yields the relation between the sintering resistance R_s and porosity p:

$$R_s = \exp[c_p(p - p_{ref})] \tag{18}$$

where $c_p = b + c_2/[2c_1 - c_2(p + p_{ref})]$ is positive. Hence, R_s positively depends on p. Note that the nature of sintering is the densification driven by surface energy, which implies that porosity can be regarded as the intrinsic parameter of sintering. Thus, to some degree the proposed R_s reflects the nature of sintering.

By plotting R_s values with given Young's modulus and thermal conductivity ratios, the distribution surface in three-dimensional coordinate system can be obtained, as shown in Fig. 6. The ratios of E_{ref}/E and λ_{ref}/λ are respectively in ranges of [1.00, 1.16] and [1.00, 1.12], determined by experimental results. It is shown in Fig. 6 that these two relative parameters have comparable contributions to R_s. Moreover, the surface is approximately flat, indicating a quasi-linear relation of these parameters. These two characteristics make R_s a suitable parameter to comprehensively evaluate the sintering resistance.

From the discussions above, it is seen that R_s is related to mechanical and thermal properties of TBCs. According to Eq. (15), R_s is greater than 1.0, if E_{ref}/E or λ_{ref}/λ is greater than 1.0. As discussed in Section 3.5.2, experimental results show the increases of both Young's modulus and thermal conductivity during sintering. If the increase of the examined coating is slower than the referential one, the sintering resistance is considered to be improved. In this case, E_{ref}/E or $\exp[(\lambda_{ref} - \lambda)/(\lambda_{ref} + \lambda)]$ is greater than 1.0. Hence, $R_s > 1.0$. Improvement of sintering resistance is determined if $R_s > 1.0$, and vice versa. In brief, R_s is a potential parameter to evaluate the sintering resistance of TBCs.

The sintering resistance of graded porous TBCs (Model-N), predicted by the proposed evaluation parameter R_s (Eq. (15)), is plotted in Fig. 7, together with conventional evaluation parameters of E_{ref}/E and λ_{ref}/λ. All the parameters are greater than 1.0 at first, demonstrating improved mechanical and thermal performances of the graded porous coating, comparing to the homogenous porous one. Sintering resistance values gradually fall to 1.0 as coatings become densified under the effect of sintering. The value of E_{ref}/E is slightly lower than 1.0 in the late stage of sintering experiment, which might be attributed to the experimental scatter. The increase of the λ_{ref}/λ value in the late stage is due to the relatively slow thermal degradation of the graded porous coating, as discussed in Section 3.5.2. Note that the R_s value is the highest throughout the annealing treatment, according to finite element analyses. The combination effect of R_s enables the observation of slight difference in sintering resistance. More importantly, it narrows deviations in separate experimental measurements for statistical reasons, as shown in Table 2. Consequently, the experimental and numerical results of R_s agree well with each other.

Another advantage of the proposed R_s is the flexibility. Different engineering applications require various properties of TBCs. For example, strain tolerance is of significance for coatings applied on rotating and stationary blades, while thermal insulation may be more important to the application in combustion chamber. According to practical operating conditions, weights of the mechanical and thermal portions can be adjusted by coefficients of w_E and w_λ in the following equation:

$$R_s^w = \left(\frac{E_{ref}}{E}\right)^{w_E} \exp\left(w_\lambda \frac{\lambda_{ref} - \lambda}{\lambda_{ref} + \lambda}\right) \tag{19}$$

The relation between modified sintering resistance R_s^w and porosity p can be similarly derived:

$$R_s^w = \exp[c_p^w(p - p_{ref})] \tag{20}$$

with $c_p^w = w_E b + w_\lambda c_2/[2c_1 - c_2(p + p_{ref})]$, showing a linear combination of mechanical and thermal weight coefficients. Consequently, similar properties can be expected in the modified evaluation parameter for sintering resistance, comparing to the original one. The flexibility of the proposed R_s expands the scope of engineering application. In conclusion, the criterion based on R_s is appropriate for comprehensive evaluation of sintering resistance.

4.2. Sintering resistance in service condition

TBCs generally works in graded temperature field in service condition. Limited by experimental facilities, studies of sintering resistance

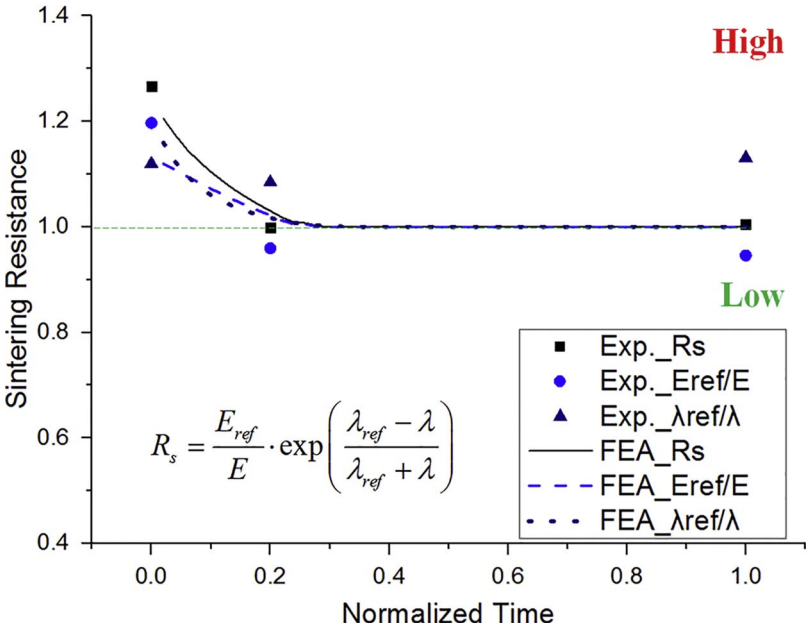

Fig. 7. Comparisons of the proposed parameter for the evolution of sintering resistance (R_s) with conventional parameters of E_{ref}/E and λ_{ref}/λ at different normalized time during the sintering of graded porous TBCs (Model-N), by experiments (Exp.) and finite element analyses (FEA).

Table 2
Difference between experimentally measured and numerically predicted sintering resistance of graded porous TBCs (Model-N).

	Difference in sintering resistance between experiment and FEA (%)		
	0 h	10 h	50 h
R_s	5.07	−3.05	0.54
E_{ref}/E	6.93	−6.14	−5.44
λ_{ref}/λ	−3.47	6.70	13.07

are performed in uniform temperature field in previous sections. In this section, evolution of R_s during annealing treatment in graded temperature field is analyzed by the finite element method presented in Section 2.2.

Evolution of sintering resistance R_s (Eq. (15)), in both uniform and graded temperature fields, is plotted in Fig. 8. Graded porous coatings exhibit better sintering resistance than the homogenous one regardless of thermal boundary conditions, seeing that R_s is generally above 1.0. Sintering behaviors of two types of graded porous coatings are identical in isothermal annealing treatment, while porosity gradient has an evident effect in graded temperature field. Sintering resistance of the TBCs with porosity increasing from top to bottom degrades slower, since the dense top sublayer is sacrificed to protect the porous bottom one from high temperature and severe sintering. Recall that the upper boundary is fixed to be 1300 °C and a constant heat flux is applied at the lower boundary, in order to simulate the service condition, as mentioned in Section 2.2. Heat transfer analyses suggest that the lowest temperature of about 1200 °C appears at bottom in the beginning stage of sintering, schematically shown in Fig. 8. The temperature reduction, due to the introduction of TBCs, is around 100 °C, which is in agreement with previous reports [1,48]. Therefore, average temperature is around 1250 °C in graded temperature field, being approximately 50 °C higher than that of uniform temperature field. By reason of elevated temperature level, R_s reduces faster in graded temperature field.

In service condition, interfacial delamination is largely responsible for the premature failure of TBCs [59–61]. It is strongly related to the stress state. Compressive stress at the interface between TC and BC is

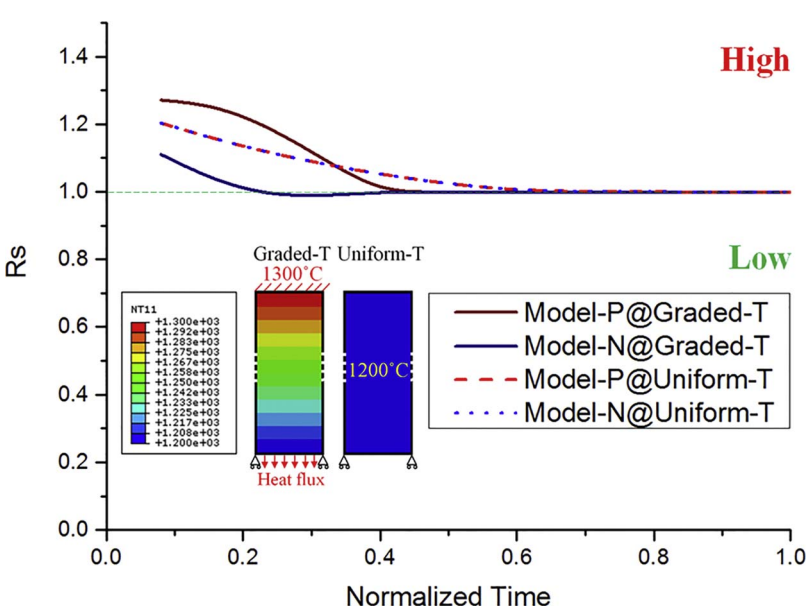

Fig. 8. Evolution of sintering resistance (R_s) of TBCs with positive and negative porosity gradients in both graded and uniform temperature fields.

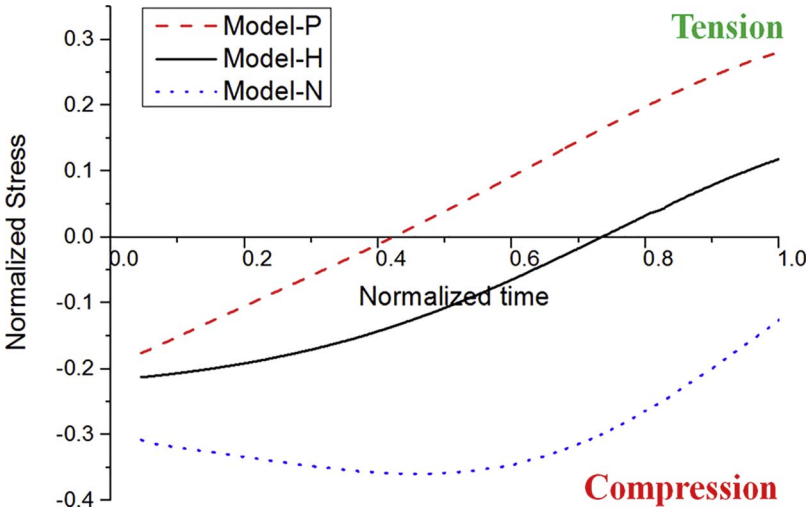

Fig. 9. Evolution of stress state at the bottom of graded and homogenous porous coatings in the graded temperature field.

considered beneficial to the lifetime of TBCs [62–65]. Stress evolution at the bottom of TC is extracted from finite element analyses, as shown in Fig. 9. In graded temperature field, compressive stress state is observed throughout the annealing treatment process in Model-N before the coating is fully sintered. However, stress state at the bottom of Model-P evolves from initially compression to tension in a relatively short period. The stress state transition is induced by the competition of sintering and thermal stress. Temperature drop from top to bottom results in compressive stress at bottom. Lower porosity level (higher relative density) leads to elevated sintering stress, which is compressive [21]. Both thermal and sintering stresses are favorable to maintain a compressive stress state in Model-N, considering the denser microstructure at bottom. In the case of Model-P with the inverted microstructure, sintering stress distribution causes tensile stress at bottom, which counteracts the effect of temperature gradient. Along with the densification induced by sintering, thermal conductivity rises and temperature gradient declines. The effect of thermal stress diminishes, leading to stress state transition in Model-P. In brief, coatings with decreasing porosity from top to bottom may exhibit better resistance to interfacial delamination and prolonged lifetime in service condition. Relevant experiments may be carried out in the future, using tube furnace for service condition simulation and digital image correlation system for strain/stress measurement.

It is seen from Fig. 8 that sintering resistance is improved by introducing porosity gradient, though the improvement of the coating with decreasing porosity from top to bottom (Model-N) is not as much as the coating with inverted microstructure (Model-P). It is seen from Fig. 9 that the interfacial stress in Model-N is lower than Model-P and keeps a compressive stress state in graded temperature field, which is favorable to avoid interfacial delamination. Consequently, the graded porous coating with porosity decreasing from top to bottom (Model-N) is recommended for engineering application.

5. Conclusions

Herein, microstructures with porosity gradient were proposed towards the enhanced sintering resistance of TBCs, which were fabricated and analyzed by using finite element method based on fully coupled thermo-mechanical framework. Various experiments including scanning electron microscopy, three-point bending test and laser-flash analysis were employed to characterize sintering induced degradations. The concluding remarks are as follows:

(1) In the present case, the Young's moduli and thermal conductivities of the graded coatings were approximately 10% lower than the homogenous one, indicated by both finite element analyses and experimental results. Hence, improved strain tolerance and thermal insulation can be expected in graded porous coatings.
(2) Taking both mechanical and thermal performances into consideration, we proposed a comprehensive parameter for evaluating the sintering resistance of TBCs, which not only reflects the nature of sintering, but also suits engineering applications.
(3) Graded porous coatings exhibited promising sintering resistance in both uniform and graded temperature fields, while the one with decreasing porosity from top to bottom demonstrated compressive stress state at interface, suggesting favorable delamination resistant and prolonged lifetime in service condition.

Acknowledgements

This work is supported by China 973 Program (2013CB035701) and NSFC (11472204, 1171101165). The authors are grateful to Prof. Leilei Zhang at NWPU for his help with thermal conductivity measurement. Thanks are also due to the help of Mr. Peng Jiang and Mr. Feng Xie at XJTU for the microstructure characterization and three-point bending tests.

References

[1] N.P. Padture, M. Gell, E.H. Jordan, Thermal barrier coatings for gas-turbine engine applications, Science 296 (2002) 280–284.
[2] N. Fleck, A. Cocks, S. Lampenscherf, Thermal shock resistance of air plasma sprayed thermal barrier coatings, J. Eur. Ceram. Soc. 34 (2014) 2687–2694.
[3] R. Vassen, A. Stuke, D. Stöver, Recent developments in the field of thermal barrier coatings, J. Therm. Spray Technol. 18 (2009) 181–186.
[4] A. Cipitria, I.O. Golosnoy, T.W. Clyne, A sintering model for plasma-sprayed zirconia TBCs. Part I: free-standing coatings, Acta Mater. 57 (2009) 980–992.
[5] A. Cipitria, I.O. Golosnoy, T.W. Clyne, A sintering model for plasma-sprayed zirconia thermal barrier coatings. Part II: coatings bonded to a rigid substrate, Acta Mater. 57 (2009) 993–1003.
[6] A. Cipitria, I.O. Golosnoy, T.W. Clyne, Sintering kinetics of plasma-sprayed zirconia TBCs, J. Therm. Spray Techn. 16 (2007) 809–815.
[7] I.O. Golosnoy, S.A. Tsipas, T.W. Clyne, An analytical model for simulation of heat flow in plasma-sprayed thermal barrier coatings, J. Therm. Spray Technol. 14 (2005) 205–214.
[8] S.A. Tsipas, I.O. Golosnoy, T.W. Clyne, R. Damani, The effect of a high thermal gradient on sintering and stiffening in the top coat of a thermal barrier coating system, J. Therm. Spray Technol. 13 (2004) 370–376.
[9] F. Cernuschi, I. Golosnoy, P. Bison, A. Moscatelli, R. Vassen, H.-P. Bossmann, S. Capelli, Microstructural characterization of porous thermal barrier coatings by IR gas porosimetry and sintering forecasts, Acta Mater. 61 (2013) 248–262.
[10] R. Vaßen, N. Czech, W. Mallener, W. Stamm, D. Stöver, Influence of impurity content and porosity of plasma-sprayed yttria-stabilized zirconia layers on the sintering behaviour, Surf. Coat. Technol. 141 (2001) 135–140.
[11] F. Cernuschi, L. Lorenzoni, S. Ahmaniemi, P. Vuoristo, T. Mäntylä, Studies of the sintering kinetics of thick thermal barrier coatings by thermal diffusivity measurements, J. Eur. Ceram. Soc. 25 (2005) 393–400.
[12] F. Cernuschi, P.G. Bison, S. Marinetti, P. Scardi, Thermophysical, mechanical and microstructural characterization of aged free-standing plasma-sprayed zirconia

coatings, Acta Mater. 56 (2008) 4477–4488.
[13] X. Cao, R. Vassen, F. Tietz, D. Stoever, New double-ceramic-layer thermal barrier coatings based on zirconia–rare earth composite oxides, J. Eur. Ceram. Soc. 26 (2006) 247–251.
[14] R. Vassen, F. Traeger, D. Stöver, New thermal barrier coatings based on pyrochlore/YSZ double-layer systems, Int. J. Appl. Ceram. Tec. 1 (2004) 351–361.
[15] R. Gadow, M. Lischka, Lanthanum hexaaluminate—novel thermal barrier coatings for gas turbine applications—materials and process development, Surf. Coat. Technol. 151 (2002) 392–399.
[16] R. Lima, B. Marple, Toward highly sintering-resistant nanostructured ZrO2-7 wt.% Y2O3 coatings for TBC applications by employing differential sintering, J. Therm. Spray Technol. 17 (2008) 846–852.
[17] R. Lima, B. Marple, Nanostructured YSZ thermal barrier coatings engineered to counteract sintering effects, Mater. Sci. Eng. A 485 (2008) 182–193.
[18] X. Chen, L. Gu, B. Zou, Y. Wang, X. Cao, New functionally graded thermal barrier coating system based on $LaMgAl_{11}O_{19}$/YSZ prepared by air plasma spraying, Surf. Coat. Technol. 206 (2012) 2265–2274.
[19] P. Carpio, E. Bannier, M. Salvador, R. Benavente, E. Sánchez, Multilayer and particle size-graded YSZ coatings obtained by plasma spraying of micro-and nanostructured feedstocks, J. Therm. Spray Technol. (2014) 1–11.
[20] C. Ramachandran, V. Balasubramanian, P. Ananthapadmanabhan, V. Viswabaskaran, Influence of the intermixed interfacial layers on the thermal cycling behaviour of atmospheric plasma sprayed lanthanum zirconate based coatings, Ceram. Int. 38 (2012) 4081–4096.
[21] B.W. Lv, H. Xie, R. Xu, X.L. Fan, W.X. Zhang, T.J. Wang, Effects of sintering and mixed oxide growth on the interface cracking of air-plasma-sprayed thermal barrier coating system at high temperature, Appl. Surf. Sci. 360 (2016) 461–469.
[22] T. Liu, S.W. Yao, L.S. Wang, G.J. Yang, C.X. Li, C.J. Li, Plasma-sprayed thermal barrier coatings with enhanced splat bonding for CMAS and corrosion protection, J. Therm. Spray Technol. 25 (2016) 213–221.
[23] G. Moskal, L. Swadźba, T. Rzychoń, Measurement of residual stress in plasma-sprayed TBC with a gradient of porosity and chemical composition, J. Achiev. Mater. Manuf. Eng. 23 (2007) 31–34.
[24] A. Portinha, V. Teixeira, J. Carneiro, J. Martins, M. Costa, R. Vassen, D. Stoever, Characterization of thermal barrier coatings with a gradient in porosity, Surf. Coat. Technol. 195 (2005) 245–251.
[25] L. Swadźba, G. Moskal, B. Mendala, M. Hetmańczyk, Characterization of microstructure and properties of TBC systems with gradient of chemical composition and porosity, Arch. Metall. Mater. 53 (2008) 945–954.
[26] S. Suresh, A. Mortensen, Fundamentals of Functionally Graded Materials, IOM Communications Ltd., London, 1988.
[27] L.S. Ma, T.J. Wang, Nonlinear bending and post-buckling of a functionally graded circular plate under mechanical and thermal loadings, Int. J. Solids Struct. 40 (2003) 3311–3330.
[28] L.S. Ma, T.J. Wang, Relationships between axisymmetric bending and buckling solutions of FGM circular plates based on third-order plate theory and classical plate theory, Int. J. Solids Struct. 41 (2004) 85–101.
[29] Z.S. Shao, T.J. Wang, Three-dimensional solutions for the stress fields in functionally graded cylindrical panel with finite length and subjected to thermal/mechanical loads, Int. J. Solids Struct. 43 (2006) 3856–3874.
[30] Z.S. Shao, T.J. Wang, K.K. Ang, Transient thermo-mechanical stresses in functionally graded cylindrical panels, AIAA J. 45 (2007) 2487–2496.
[31] A. Evans, Structural and microstructural design in brittle materials, Proc. DARPA/AFML Rev. Prog. in Quant. NDE 89 (1980).
[32] O. Borrero-López, A.L. Ortiz, F. Guiberteau, N.P. Padture, Microstructural design of sliding-wear-resistant liquid-phase-sintered SiC: an overview, J. Eur. Ceram. Soc. 27 (2007) 3351–3357.
[33] J.M. Gere, Mechanics of Materials, sixth ed., Brooks/Cole, CA, 2004.
[34] L. Yang, Z.C. Zhong, J. You, Q.M. Zhang, Y.C. Zhou, W.Z. Tang, Acoustic emission evaluation of fracture characteristics in thermal barrier coatings under bending, Surf. Coat. Technol. 232 (2013) 710–718.
[35] J.H. Lienhard IV, J.H. Lienhard V, A Heat Transfer Textbook, third ed., Phlogiston Press, MA, 2001.
[36] A. Bejan, A.D. Kraus, Heat Transfer Handbook, John Wiley & Sons NJ, 2003.
[37] M. Gasik, B. Zhang, A constitutive model and FE simulation for the sintering process of powder compacts, Comp. Mater. Sci. 18 (2000) 93–101.
[38] T.G. Fox Jr., P.J. Flory, Viscosity—molecular weight and viscosity—temperature relationships for polystyrene and polyisobutylene, J. Am. Chem. Soc. 70 (1948) 2384–2395.
[39] L. An, R. Riedel, C. Konetschny, H. Kleebe, R. Raj, Newtonian viscosity of amorphous silicon carbonitride at high temperature, J. Am. Ceram. Soc. 81 (1998) 1349–1352.
[40] M. Ahrens, R. Vaßen, D. Stöver, S. Lampenscherf, Sintering and creep processes in plasma-sprayed thermal barrier coatings, J. Therm. Spray Techn. 13 (2004) 432–442.
[41] P. Scardi, M. Leoni, F. Cernuschi, A. Figari, Microstructure and heat transfer phenomena in ceramic thermal barrier coatings, J. Am. Ceram. Soc. 84 (2001) 827–835.
[42] S. Raghavan, H. Wang, R.B. Dinwiddie, W.D. Porter, M.J. Mayo, The effect of grain size, porosity and yttria content on the thermal conductivity of nanocrystalline zirconia, Scripta Mater. 39 (1998) 1119–1125.
[43] W. Chi, S. Sampath, H. Wang, Microstructure–thermal conductivity relationships for plasma-sprayed yttria-stabilized zirconia coatings, J. Am. Ceram. Soc. 91 (2008) 2636–2645.
[44] A. Bjorneklett, L. Haukeland, J. Wigren, H. Kristiansen, Effective medium theory and the thermal conductivity of plasma-sprayed ceramic coatings, J. Mater. Sci. 29 (1994) 4043–4050.
[45] X.L. Fan, R. Xu, W.X. Zhang, T.J. Wang, Effect of periodic surface cracks on the interfacial fracture of thermal barrier coating system, Appl. Surf. Sci. 258 (2012) 9816–9823.
[46] W.X. Zhang, T.J. Wang, L.X. Li, Numerical analysis of the transverse strengthening behavior of fiber-reinforced metal matrix composites, Comp. Mater. Sci. 39 (2007) 684–696.
[47] E.P. Busso, J. Lin, S. Sakurai, M. Nakayama, A mechanistic study of oxidation-induced degradation in a plasma-sprayed thermal barrier coating system. Part I: model formulation[J], Acta Mater. 49 (9) (2001) 1515–1528.
[48] J. Thompson, T. Clyne, The effect of heat treatment on the stiffness of zirconia top coats in plasma-sprayed TBCs, Acta Mater. 49 (2001) 1565–1575.
[49] M. Shinozaki, T. Clyne, A methodology based on sintering-induced stiffening, for prediction of the spallation lifetime of plasma-sprayed coatings, Acta Mater. 61 (2013) 579–588.
[50] G. Moskal, L. Swadźba, M. Hetmańczyk, B. Witala, B. Mendala, J. Mendala, P. Sosnowy, Characterization of microstructure and thermal properties of $Gd_2Zr_2O_7$-type thermal barrier coating, J. Eur. Ceram. Soc. 32 (2012) 2025–2034.
[51] A.K. Rai, M.P. Schmitt, R.S. Bhattacharya, D. Zhu, D.E. Wolfe, Thermal conductivity and stability of multilayered thermal barrier coatings under high temperature annealing conditions, J. Eur. Ceram. Soc. 35 (2015) 1605–1612.
[52] X.L. Fan, R. Xu, T.J. Wang, Interfacial delamination of double-ceramic-layer thermal barrier coating system, Ceram. Int. 40 (2014) 13793–13802.
[53] B. Siebert, C. Funke, R. Vaβen, D. Stöver, Changes in porosity and Young's Modulus due to sintering of plasma sprayed thermal barrier coatings, J. Mater. Process. Technol. 92 (1999) 217–223.
[54] S. Paul, A. Cipitria, I. Golosnoy, L. Xie, M. Dorfman, T. Clyne, Effects of impurity content on the sintering characteristics of plasma-sprayed zirconia, J. Therm. Spray Technol. 16 (2007) 798–803.
[55] B.W. Lv, X.L. Fan, H. Xie, T.J. Wang, Effect of neck formation on the sintering of air-plasma-sprayed thermal barrier coating system, J. Eur. Ceram. Soc. 37 (2017) 811–821.
[56] A. Shinmi, X. Zhao, P. Xiao, Mechanical and electrical characterisation of a phase transformation in thermal barrier coatings, Surf. Coat. Technol. 205 (2010) 2678–2686.
[57] H.-J. Rätzer-Scheibe, U. Schulz, The effects of heat treatment and gas atmosphere on the thermal conductivity of APS and EB-PVD PYSZ thermal barrier coatings, Surf. Coat. Technol. 201 (2007) 7880–7888.
[58] Q. Yu, A. Rauf, N. Wang, C. Zhou, Thermal properties of plasma-sprayed thermal barrier coating with bimodal structure, Ceram. Int. 37 (2011) 1093–1099.
[59] R. Xu, X.L. Fan, W.X. Zhang, Y. Song, T.J. Wang, Effects of geometrical and material parameters of top and bond coats on the interfacial fracture in thermal barrier coating system, Mater. Des. 47 (2013) 566–574.
[60] R. Xu, X.L. Fan, W.X. Zhang, T.J. Wang, Interfacial fracture mechanism associated with mixed oxides growth in thermal barrier coating system, Surf. Coat. Technol. 253 (2014) 139–147.
[61] X.L. Fan, W. Jiang, J. Li, T. Suo, T.J. Wang, R. Xu, Numerical study on interfacial delamination of thermal barrier coatings with multiple separations, Surf. Coat. Technol. 244 (2014) 117–122.
[62] R. Vaßen, G. Kerkhoff, D. Stöver, Development of a micromechanical life prediction model for plasma sprayed thermal barrier coatings, Mater. Sci. Eng. A 303 (2001) 100–109.
[63] K. Sfar, J. Aktaa, D. Munz, Numerical investigation of residual stress fields and crack behavior in TBC systems, Mater. Sci. Eng. A 333 (2002) 351–360.
[64] V. Teixeira, M. Andritschky, W. Fischer, H. Buchkremer, D. Stöver, Effects of deposition temperature and thermal cycling on residual stress state in zirconia-based thermal barrier coatings, Surf. Coat. Technol. 120 (1999) 103–111.
[65] A.K. Ray, R.W. Steinbrech, Crack propagation studies of thermal barrier coatings under bending, J. Eur. Ceram. Soc. 19 (1999) 2097–2109.